

Thermally Activated Point-Defects Diffusion in Methylammonium Lead Trihalide: Anisotropic and Ultra-High Mobility of Iodine

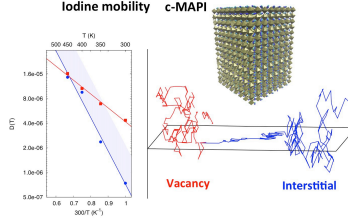
P. Delugas, C. Caddeo, A. Filippetti, and A. Mattoni*

Istituto Officina dei Materiali, CNR-IOM SLACS Cagliari, 09042 Monserrato (CA)

E-mail: mattoni@iom.cnr.it

Abstract

We study the diffusion of point-defects in crystalline MAPI at finite temperatures by using all-atoms molecular dynamics. We find that, for what concerns intrinsic defects, iodine diffusion is by far the dominant mechanism of ionic transport in MAPI with diffusivities as high as $7.4 \cdot 10^{-7}$ and $4.3 \cdot 10^{-6} \text{ cm}^2\text{s}^{-1}$ at 300 K and single activation energies of 0.24 eV and 0.10 eV, for interstitials and vacancies, respectively. The comparison with common covalent and oxide crystals reveals the ultra-high mobility of defects in MAPI. Though at room temperature the vacancies are about one order of magnitude more diffusive, the anisotropic interstitial dynamics increases more rapidly with temperature and it can be dominant at high temperatures. Present results are fully consistent with the involvement of iodide ions in hysteresis and have implications for the improvement of the material quality by a better control of defects diffusion.



Point-defects are of paramount importance in organic-inorganic lead halide perovskites, recently emerged as record-high efficient class of hybrid materials for solar cells.¹ The exceptional optoelectronic and photovoltaic properties of such hybrid semiconductors (e.g. methylammonium lead halide $\text{CH}_3\text{NH}_3\text{PbI}_3$, MAPI)²⁻⁴ are unexpected considering that high concentration of point defects^{5,6} and structural disorder (e.g. grain boundaries) are abundant in ionic⁷ and solution-processed materials.⁸

This seeming paradox, that shows the importance of understanding defects in MAPI, has been explained in terms of the resilience of electronic properties of MAPI to defects:^{5,9} the bonding (anti-bonding) nature of the Pb-I conduction (valence) bands prevents the formation of deep electronic levels in the gap. With the notable exception of electronic defects due to molecular fragments¹⁰, most intrinsic defects create only shallow levels.¹⁰⁻¹² Also a self-regulation mechanism in which electronic defects are compensated by ionic disorder has been proposed to explain MAPI electronic resilience.⁶

Though defects are not detrimental for MAPI electronic properties, they have nevertheless dramatic effects. The most striking evidence is hysteretic current-voltage behavior observed in the timescale of 1-10⁴ seconds.¹³⁻¹⁶ As suggested by much direct and indirect experimental evidence, ion migration is at the origin or an important contributing factor for such unusual phenomenon.¹⁶⁻²⁰ Migration of ionic defects (either in the bulk or interfaces or grain boundaries)^{13,21} has been invoked also to explain switchable photovoltaic effects,²² light-induced changes in structural, dielectric and transport properties,²³ these latter indicating a large fraction of conduction due to ions.¹³ In particular, giant switchable photovoltaic effect²² proved the importance of ion migration for the photocurrent hysteresis by excluding

other possible factors such as ferroelectricity.²⁴ Though the ferroelectric nature of MAPbI₃ is still disputed with reports claiming either presence²⁵ or absence²⁶ of ferroelectricity, from a theoretical perspective, the possible ferroelectric behavior of hybrid perovskites can be hardly considered a physically sound explanation.¹⁴ Ab initio calculations give moderate polarization only at low temperature and predict the suppression of ferroelectric distortion at room temperature.²⁷ This is furthermore supported by the ascertained ability of molecular dipoles to rotate in few picoseconds^{28,29} with molecular relaxation times several orders of magnitude shorter than hysteretic transients.^{14,29} Understanding the nature and migration of point-defects is, accordingly, a fundamental problem of great technological interest for hybrid perovskites.³⁰

At equilibrium, the electrical ionic mobility μ is related to the ionic diffusivity (D) by the Nernst-Einstein equation $\mu = qD/k_B T$, with ionic charge q , Boltzmann constant k_B and absolute temperature T . However, this relation is not valid under non-equilibrium conditions (e.g. in presence of degradation phenomena) and the estimated diffusion coefficients depend on the adopted model. High values of $10^{-8} - 10^{-7} \text{ cm}^2\text{s}^{-1}$ have been obtained from voltage transient measurements by Yang et al.¹³ though other reports, based on the analysis of switchable photovoltaic in lateral structure devices, suggest two-orders of magnitude smaller values.³¹ The ionic diffusion could also explain the observed increase of bulk conductivity with temperature characterized by a measured activation energy of 0.43 eV,¹³ as well as the temperature dependence of the hysteretic current-voltage. The reported values (0.23,²¹0.31,²¹0.33,¹⁴0.43,¹³0.5,³²0.6 eV³³) depend on the fabrication methods and the different crystalline quality.²¹ Accordingly, experiments are convincing in terms of thermally activated ionic migration under external field but the direct evidence of long range ionic diffusion is debated and still represents an important open question.

The chemical nature of the diffusive species is equally disputed since a direct experimental evidence is missing. Most experimental studies conclude that diffusion is due to iodine defects.^{13,21} Other studies supported by atomistic simulations focus on vacancies, ei-

ther MA^{6,34} or I^{6,14} that can form as Schottky pairs through understoichiometric MAPI degradation $\emptyset = V_{MA} + V_I + MAI$. Other possibilities include iodine interstitials^{11,35} or extrinsic defects (oxygen substituting for iodine).¹³

Atomistic simulations have been extensively used to study the electronic properties of point-defects,^{5,10,35–38} however only a limited number of recent works have investigated by static methods the diffusion of elemental I,Pb,MA defects^{14,15,33,34} or hydrogens.³⁹ For iodine vacancies, the reported activation energies are quite different: 0.6 eV,³³ 0.45 eV,³⁴ 0.2 eV¹⁴ and 0.08 eV.¹⁵ Unfortunately, the straightforward simulation of the ions diffusion at finite temperature is computationally out-of-reach of ab initio methods.

In this Letter, we show that it is possible to study the diffusion of the elementary point-defects in crystalline MAPI (c-MAPI) at finite temperatures by using all-atoms molecular dynamics employing the MYP classical interatomic potential recently developed by the Authors.²⁹ We find that, for what concerns intrinsic defects, iodine diffusion (vacancies and

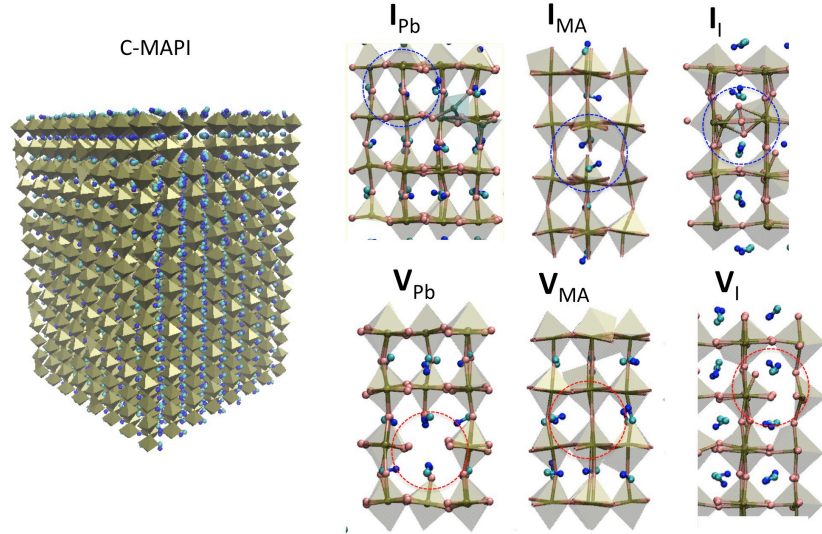


Figure 1: Sticks&balls representation of iodine interstitial in MAPI

interstitials) is by far the dominant mechanism of ionic transport in MAPI (from room up to sublimation temperature) with ultra-high diffusivities at 300 K of $7.4 \cdot 10^{-7}$ and $4.3 \cdot 10^{-6}$

cm^2s^{-1} and single migration energies of 0.24 eV and 0.1 eV, for interstitials and vacancies, respectively. These values reveal the ultra-high mobility of point-defects in MAPI compared to other covalent and oxide crystals. Though vacancies are about one order of magnitude more diffusive than interstitials, it is found that interstitial dynamics, characterized by a peculiar quasi-planar anisotropic diffusion, increases more rapidly with temperature and it can be dominant at temperatures greater than 350 K. Present results are fully consistent with the involvement of iodide ions in hysteresis and current-voltage transients and they also represent an important step forward in the modeling of the ionic response of the material at finite temperature. In particular they can have implications for the material improvement by the control of defects diffusion.

Interstitial and vacancy defects are obtained from a perfect orthorhombic crystal structure (see Figure 1) by adding (removing) one X ionic constituent among the possible choices $X=\text{MA}, \text{Pb}, \text{I}$. Simulated crystals contain 3072 atoms (256 f.u.). Larger systems were also considered to exclude size effects. Each defected crystal is first optimized and then equilibrated at different temperatures for annealing times long up to 10 ns. The variable-cell conditions (both volume and angles of the simulation box) make it possible to reproduce correctly the density of the MAPI²⁹ and to adapt the volume to the presence of the defect. Furthermore, the MYP model reproduces molecular rotations^{29,40} consistently with experiments and other ab initio calculations,^{14,28} an important agreement that represents a strong validation of the adopted force-field.

Snapshots of the defects at room temperature are reported in Figure 1. Molecular dynamics clearly shows that the iodine defects (both vacancies and interstitials) are very mobile, and several migration events are detectable in the nanosecond scale at room temperature; on the contrary no migration events are observed in the same conditions for both Pb and MA defects. This is a first important result. In agreement with previous reports¹⁴ (based on ab initio static energy barrier calculations) the timescale of the MA and Pb ions diffusion is several orders of magnitude larger than the one for iodine ions. This is also consistent

with the experiments on solid-state electrochemical cells¹³ suggesting iodine as the mobile species.

Snapshots of the iodine interstitial diffusion during the 300 K dynamics are reported in Figure 2. The defect geometry is consistent with DFT calculations for negative iodines³⁵ and it consists of a dumbbell formed by two I atoms sharing the same ideal lattice position (see blue circles in Figure 2). The migration occurs when one of the two I-Pb bonds of the defect rotates around Pb in the plane of the dumbbell kicking off a neighboring iodide ion and giving rise to a new dumbbell at a neighboring crystal site. The ability of one

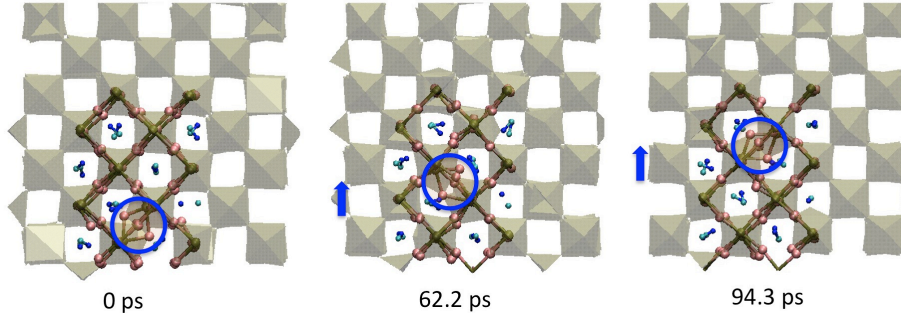


Figure 2: Snapshots of the I_I diffusion during annealing (time increases from left to right); the local crystal structure is represented together with the octahedra (Pb, I, C, N are green, pink, blue and cyan spheres; PbI octahedra are gold; H atoms of MA molecules are not represented for clarity) blue circles indicate the position of the defect and blue arrows are the displacements with respect to the previous defects positions.

point-defect to move is measured by its diffusivity D . Within transition state theory⁴¹ the T dependence of diffusivity, $D = D_0 \cdot e^{-\frac{E_m}{k_B T}}$, can be calculated from the migration energy E_m and the prefactor D_0 . These can be estimated by the configurational energy along the defect migration path at T=0 K. These calculations are affordable by ab initio methods but it is not easy to include correlations, anisotropies, entropic contributions of the real dynamics, particularly for a relatively soft material such as MAPI. Alternatively, the finite temperature MD simulations can give direct insight within the diffusion mechanism of point-defects, provided that the diffusion time and length can be reached during the simulation at that temperature.

Within the assumption that the motion can be described as a random walk, the mean square displacements (MSD) of defects at long times t increases linearly $\langle x^2 \rangle \approx Dt$ and the diffusivity corresponds to the slope $D \approx \frac{\langle x^2 \rangle}{t}$ ⁴². The formula can be expressed in terms of atomic positions $D = \lim_{t \rightarrow \infty} \frac{1}{2\mathfrak{D}n_d} \frac{1}{t} \sum_{i \in X} (\mathbf{r}_i(t) - \mathbf{r}_i(0))^2$ by averaging over all the constituents i of the chemical type X (with $X = \text{I, Pb, MA}$); n_d is the number of diffusing species ($n_d = 1$, for point-defects) and $\mathfrak{D} = 3$ is the dimensionality of the crystal containing the defect. For the same MSD, if the motion occurs in a subspace of dimension $\mathfrak{d} < 3$ the *effective diffusivity* in the subspace is increased by a factor $\frac{3}{\mathfrak{d}} \geq 1$ with respect to the three dimensional case.

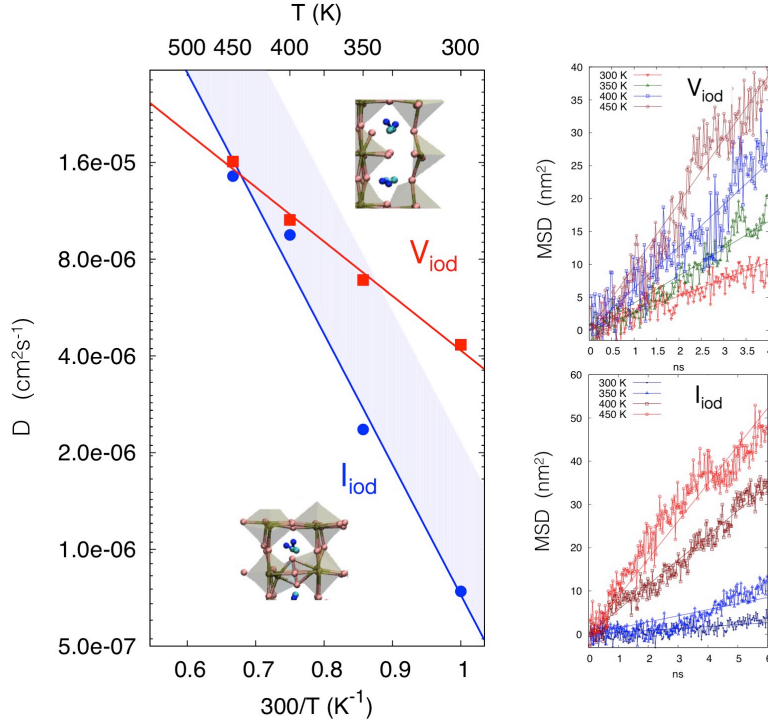


Figure 3: Mean square displacements (top right, V_I and bottom right, I_I) and Arrhenius plot (left) of vacancy (red) and interstitial (blue) obtained by MD. The shadowed region in the Arrhenius plot represents the effective interstitial mobility including the dimensional reduction of I_I diffusion, $1 \leq \mathfrak{d} \leq 3$.

The iodine MSD's at 300 K-450 K are reported in Figure 3 (right panels) for the single vacancy (top) and interstitial (bottom) defect in c-MAPI. High temperatures are relevant

for applications since they can be reached during processing or at working conditions of photovoltaic devices. We also point out that the investigated T range falls within the interval of MAPI thermal stability as obtained from thermogravimetry indicating the onset of sublimation at $T = 511$ K,⁴³ though degradation in real samples can occur at lower temperatures⁴⁴ likely due to imperfections and chemical contaminations. The atomistic results reveal that both diffusivity coefficients D_{I_I}, D_{V_I} have Arrhenius-like behavior $D_X = D_X^0 e^{-\frac{E_X}{k_B T}}$, each ($X=I_I$ or V_I) with a single migration energy E_X in the whole range of temperature investigated.

Table 1: Iodine defects diffusivity, prefactor and migration energy in crystalline MAPI compared to corresponding defects in silicon and some prototypical oxides.

	D_X (T=300 K) (cm^2s^{-1})	D_X^0 (cm^2s^{-1})	E_X (eV)
MAPI (this work)			
V_I	$4.3 \cdot 10^{-6}$	$2.05 \cdot 10^{-4}$	0.10
I_I	$7 \cdot 10^{-7}$	$8.3 \cdot 10^{-3}$	0.24
Silicon ^{45,46}			
V_{Si}	$5 \cdot 10^{-11} - 2.16 \cdot 10^{-6}$	$1.5 \cdot 10^{-3} - 1.18 \cdot 10^{-4}$	0.1 – 0.45
I_{Si}	$< 4 \cdot 10^{-16}$	$0.14 - 1.58 \cdot 10^{-1}$	0.78 – 1.37
Oxides			
$\text{SrTiO}_3(V_O)$ ⁴⁷	$< 10^{-18}$		0.93
$\text{La}_2\text{NiO}_4(I_O)$ ⁴⁸	$10^{-8} - 10^{-7}$		0.51 – 0.54
$\text{La}_{0.8}\text{Sr}_{0.2}\text{MnO}_3(O)$ ⁴⁹	$\approx 10^{-17}$	$1.2 \cdot 10^{-4}$	0.7 – 0.73
$\text{Cr}_2\text{O}_3(I_O V_O)$ ⁵⁰	10^{-17}	$4.04 \cdot 10^{-7}$	0.78 – 1.01

At room temperature the vacancy diffusivity is as high as $D_{V_I} = 4.3 \cdot 10^{-6} \text{cm}^2\text{s}^{-1}$. At the same temperature the interstitial is six times less diffusive but still characterized by a very high value $D_{I_I} = 7 \cdot 10^{-7} \text{cm}^2\text{s}^{-1}$. The higher migration energy of interstitials stands for a larger energy cost associated to its migration that is consistent with previous ab initio literature^{14,15,33,34} and physical intuition. The larger prefactor is consistent with a larger entropy and a more stiff configurational energy associated to the extra iodine atom in the interstitial case. In order to check that the results are not affected by volumetric effects, we performed additional calculations at constant volume, finding no sizable difference in the

calculated diffusivity. To further validate the molecular dynamics predictions and the model potential accuracy against ab initio results, we have performed static energy calculations for the vacancy case. We found a static energy profile that is consistent with ab initio data of Meloni et al.¹⁴ with a maximum of about 0.3 eV. Expectedly, we observe that the static barrier is higher than the dynamic one. The difference can be attributed to thermal fluctuations (included during the dynamics but not in either ab initio or classical) that reduce the actual cost of diffusion. In order to appreciate the ultra-high mobility of the iodine defects it is useful to compare the defect diffusivity of MAPI with that of oxides and covalent materials obtained with MD. Migration energies in oxides are typically larger than 0.5 eV (see table) and the oxygen diffusivities are vanishingly small at room temperature. Concerning silicon, only the vacancy has high diffusivity, that according to tight binding calculations⁴⁵ is close, though still smaller, than MAPI; conversely, interstitials are practically immobile at room temperature and have a much higher (> 1 eV) activation energy. The ultra-high diffusivity of interstitial defect in MAPI can be attributed to the smaller ionic charges of iodides (-1) against oxides (-2) and also to the larger lattice spacing, both features resulting in lower cohesive-energy density and thermodynamic stability but also in a lower cost for defect formation and migration.

The ionic mobility at equilibrium can be calculated from the diffusivity through the formula $\mu_X = q \frac{D_X}{k_B T}$, obtaining $1.72 \cdot 10^{-4} \text{cm}^2 \text{V}^{-1} \text{s}^{-1}$ and $2.8 \cdot 10^{-5} \text{cm}^2 \text{V}^{-1} \text{s}^{-1}$ for V_I and I_I , respectively. Accordingly, MAPI can be classified as mixed ion-electron conductor in agreement with conductivity measurements.¹³ Due to the higher activation energy and prefactor of interstitials, the two lines $D_{I_I}(T), D_{V_I}(T)$ have different slopes and intersect at high temperatures (the crossing temperature can be calculated to be $T = \frac{E_{I_I} - E_{V_I}}{k_B} \frac{1}{\log D_{I_I}^0 / D_{V_I}^0}$ that gives 450 K for the present case) beyond which the interstitials become more mobile than vacancies. Taken into account the actual temperature of sublimation, this occurs only for a small T window. However, the interstitials can play a role also at lower T taking into account that the diffusivity is still high and that the mechanism of iodine interstitials is

qualitatively different from V point-defects. This can be understood from the analysis of defect trajectory.

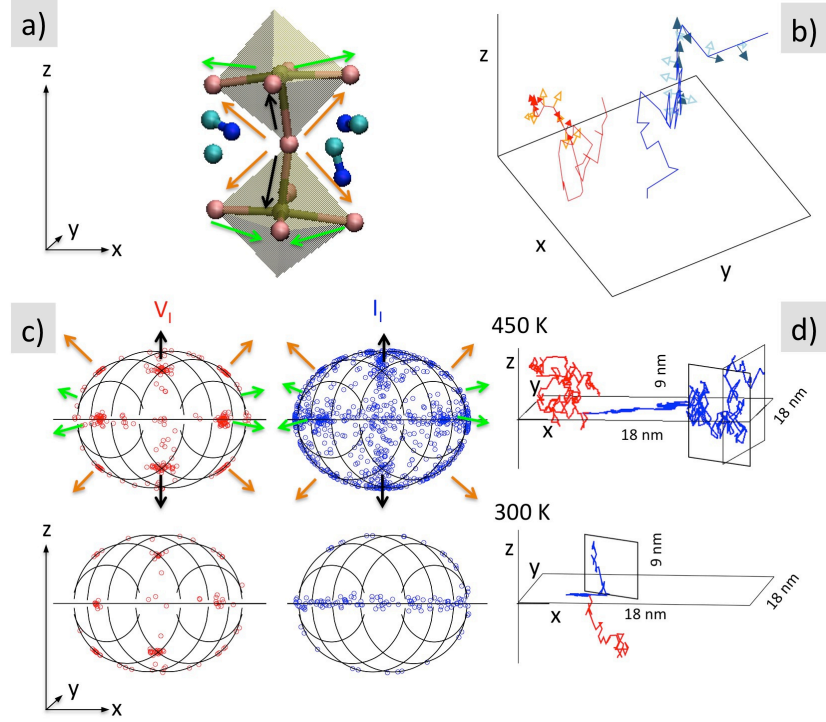


Figure 4: Analysis of the migration iodine defects: panel a) sticks&balls representation of the local MAPI crystal structure with octahedra (Pb, I, C, N are green, pink, blue and cyan spheres; PbI octahedra are transparent green) showing the apical-equatorial edges (orange and black arrows) and equatorial-equatorial edges (green arrows); panel b) portions of the V_I (red) and I_I (blue) trajectories with the local tangent vectors (empty arrows) and vectors normal to the local (osculating) plane (filled arrows); panel c) directional distribution of diffusion events (tangent vectors) represented over the spherical surface for V_I (red points) and I_I (blue points) at 450 K (top) and 300 K (bottom); panel d) V_I (red) and I_I (blue) trajectories showing the local planes of the interstitial diffusion compared to the fully isotropic diffusion of vacancies.

At each step of the MD simulations the defect position within the crystal is identified by the change in coordination-number of Pb atoms, similarly to Ref. 51; in fact, in the perfect c-MAPI the Pb atoms are at the center of PbI tetrahedra with six-fold coordination while in presence of a neighboring vacancy (interstitial) they become under (over-) coordinated. It is possible to reconstruct the trajectory of iodine defects by identifying the positions of

the Pb atoms with modified coordination. In Figure 4b, small portions of the trajectory of interstitial (blue) and vacancy (red) are reported. The vectors tangent to the trajectory (filled arrows) represent the defect displacement at each position, i.e. the direction of the local migration. The tangents τ_t (determining the direction of the jump at time t) can be normalized $\hat{\tau}_t$ and represented as unit vectors pointing to the surface of a unit sphere (see panel 4c). Each point represents a diffusion event along the corresponding crystallographic direction. The whole set of points taken during the whole dynamics gives rise to a directional distribution of diffusion events. In panel 4c we report the cases of interstitials (blue) and vacancies (red) at T=300K (bottom) and 450K (top). Let us focus first on the vacancy at 300 K.

The distribution reveals that the diffusion events occur along all the high symmetry crystallographic directions of MAPI (points over the sphere where symbols accumulate) corresponding to displacements along the possible edges of PbI octahedra (see Figure 4a). Orange and black arrows in panels 4a and 4c refer to apical-equatorial migrations; green arrows to equatorial-equatorial jumps. At 450 K the diffusivity and the number of migration events increase with respect to 300 K; however the distribution is qualitatively invariant. By time averaging $\hat{\tau}_t$ we can verify that opposite directions are explored with equal probability ($\langle \hat{\tau} \rangle \simeq 0$). Furthermore the inertia moments $\langle \hat{\tau}_\alpha^2 \rangle$ along Cartesian directions indicates that the distribution is quite isotropic, i.e. $\langle \tau_\alpha^2 \rangle / \langle \tau_\beta^2 \rangle \simeq 1$ ($\alpha, \beta = x, y, z$) within statistical errors (30% at T=300 K and 5% at 450 K).

We conclude that in the whole range of temperatures, the vacancies give rise to a three dimensional uncorrelated brownian motion.

The picture is qualitatively different for interstitials. Let us focus first on 450 K. Since the interstitials induce larger local distortions than vacancies, a larger standard deviation is found around the high symmetry directions in the spherical surface. However, at 300 K it can be appreciated a more qualitative difference between I_I and V_I in the same simulation time. The I_I directional distribution clearly shows accumulation in the (001) crystallographic

plane, i.e. the defect tends to remain in the plane containing the dumbbell. This means that the planar defect structure of I_I , at variance with V_I , is able to locally break the symmetry of the crystal introducing a preferential plane for migration. This has been quantitatively analyzed by calculating the local plane of the trajectory (corresponding to the osculating circle of a continuous curve), defined as the cross vector of two consecutive tangents $\hat{n}_t = \hat{\tau}_t \times \hat{\tau}_{t+dt}$. Empty arrows are used in Figure 4b to represent the local planes along the defects trajectories. Though the defect plane is able to change direction during the simulation, nevertheless a clear tendency to stay constant is observed. This can be quantified by the planar correlation time $\langle \hat{n}_0 \cdot \hat{n}_t \rangle$ that is found to be in the time scale of tens of nanoseconds at 300 K. The correlation time decreases by almost one order of magnitude from 300 K to 450 K. Conversely, the planar correlation time of V_I is smaller than 0.1 ns at all studied temperatures, so practically discardable. We can speculate that, at least at short time scales, the effective interstitial diffusivity and its role in ionic transients is enhanced.

The calculated diffusivity provides a measure of the distance that anions can explore in the time scale of hysteretic transients. By using the relation $\lambda_X = \sqrt{D_X \tau}$ and using $\tau = 1$ s we calculate $\lambda_{V_I} \approx 20 \mu\text{m}$ and $\lambda_{I_I} \approx 2.5 \mu\text{m}$ at 300 K. At 400 K both increase and approach similar values (32 μm and 30 μm , respectively). The predicted diffusion time for 0.6 mm film thickness¹³ is calculated to be of the order of 10^2 s and 10^4 s, for vacancies and interstitials, respectively in qualitative agreement with experiments also considering that we are discarding defects interactions.¹³

In conclusion, we find that, for what concerns intrinsic defects, iodine diffusion (vacancies and interstitials) is by far the dominant mechanism of ionic transport in MAPI from room to sublimation temperature (300-450 K) with ultra-high diffusivities ($7 \cdot 10^{-7}$ and $4 \cdot 10^{-6} \text{ cm}^2 \text{ s}^{-1}$ at 300 K for interstitials and vacancies, respectively) and single activation energies of 0.1 eV and 0.24 eV, respectively. At room temperature, the vacancies are about one order of magnitude more diffusive than interstitials; nevertheless the interstitial dynamics is unusually fast and it further reveals quasi planar trajectories consistent with correlation times in the

nanosecond scale corresponding to a higher effective diffusivity in the ultrashort time scale. The calculated interstitial anisotropies also suggest the possibility to modify the diffusivity of V_I, I_I by external strain or by material texturization possibly opening novel strategies for defects management.

Overall, present results are fully consistent with the involvement of iodine defects in hysteresis and transients in current-voltage characteristics. The calculation of the intrinsic diffusivity of iodine defects is an important step forward to develop a comprehensive modeling of the material at working conditions or under electric fields.

Acknowledgements

A.M. thanks Simone Meloni for useful discussions and for providing ab initio data on migration energy path. We acknowledge financial support by Istituto Italiano di Tecnologia under Project CompuNet, by Regione Autonoma della Sardegna (CRP-24978 and CRP-18013), by Fondazione Banco di Sardegna (Project 7454, 5794). We acknowledge computational support by CINECA, Italy through IS CRA Project VIPER and THESTA.

References

- (1) Lee, M. M.; Teuscher, J.; Miyasaka, T.; Murakami, T. N.; Snaith, H. J. Efficient Hybrid Solar Cells Based on Meso-Superstructured Organometal Halide Perovskites. *Science* **2012**, *338*, 643–7.
- (2) Filippetti, A.; Mattoni, A. Hybrid Perovskites for Photovoltaics: Insights from First Principles. *Phys. Rev. B* **2014**, *89*, 125203.
- (3) Burschka, J.; Pellet, N.; Moon, S.-J.; Humphry-Baker, R.; Gao, P.; Nazeeruddin, M. K.; Grätzel, M. Sequential Deposition as a Route to High-Performance Perovskite-Sensitized Solar Cells. *Nature* **2013**, *499*, 316–9.

- (4) Polman, A.; Knight, M.; Garnett, E. C.; Ehrler, B.; Sinke, W. C. Photovoltaic Materials: Present Efficiencies and Future Challenges. *Science* **2016**, *352*.
- (5) Kim, J.; Lee, S.-H.; Lee, J. H.; Hong, K.-H. The Role of Intrinsic Defects in Methylammonium Lead Iodide Perovskite. *J. Phys. Chem. Lett.* **2014**, *5*, 1312–1317.
- (6) Walsh, A.; Scanlon, D. O.; Chen, S.; Gong, X. G.; Wei, S.-H. Self-Regulation Mechanism for Charged Point Defects in Hybrid Halide Perovskites. *Angew. Chemie Int. Ed.* **2015**, *54*, 1791–1794.
- (7) Goodenough, J. B. Electronic and Ionic Transport Properties and Other Physical Aspects of Perovskites. *Reports Prog. Phys.* **2004**, *67*, 1915–1993.
- (8) Peng, W.; Anand, B.; Liu, L.; Sampat, S.; Bearden, B. E.; Malko, A.; Chabal, Y. J. Influence of Growth Temperature on Bulk and Surface Defects in Hybrid Lead Halide Perovskite Films. *Nanoscale* **2015**, 1627–1634.
- (9) Zakutayev, A.; Caskey, C. M.; Fioretti, A. N.; Ginley, D. S.; Vidal, J.; Stevanovic, V.; Tea, E.; Lany, S. Defect Tolerant Semiconductors for Solar Energy Conversion. *J. Phys. Chem. Lett.* **2014**, *5*, 1117–1125.
- (10) Delugas, P.; Filippetti, A.; Mattoni, A. Methylammonium Fragmentation in Amines as Source of Localized Trap Levels and the Healing Role of Cl in Hybrid Lead-Iodide Perovskites. *Phys. Rev. B* **2015**, *92*, 045301.
- (11) Yin, W.-J.; Shi, T.; Yan, Y. Unusual Defect Physics in $\text{CH}_3\text{NH}_3\text{PbI}_3$ Perovskite Solar Cell Absorber. *Appl. Phys. Lett.* **2014**, *104*, 063903.
- (12) Yin, W.-J.; Shi, T.; Yan, Y. Unique Properties of Halide Perovskites as Possible Origins of the Superior Solar Cell Performance. *Adv. Mater.* **2014**, 4653–4658.

- (13) Yang, T.-y.; Gregori, G.; Pellet, N.; Grätzel, M.; Maier, J. The Significance of Ion Conduction in a Hybrid Organic-Inorganic Lead-Iodide-Based Perovskite Photosensitizer. *Angew. Chemie Int. Ed.* **2015**, *54*, 7905–7910.
- (14) Meloni, S.; Moehl, T.; Tress, W.; Franckevičius, M.; Saliba, M.; Lee, Y. H.; Gao, P.; Nazeeruddin, M. K.; Zakeeruddin, S. M.; Rothlisberger, U. et al. Ionic Polarization-Induced Current-Voltage Hysteresis in $\text{CH}_3\text{NH}_3\text{PbX}_3$ Perovskite Solar Cells. *Nat. Commun.* **2016**, *7*, 10334.
- (15) Azpiroz, J. M.; Mosconi, E.; Bisquert, J.; De Angelis, F. Defect Migration in Methylammonium Lead Iodide and its Role in Perovskite Solar Cell Operation. *Energy Environ. Sci.* **2015**, *8*, 2118–2127.
- (16) Snaith, H. J.; Abate, A.; Ball, J. M.; Eperon, G. E.; Leijtens, T.; Noel, N. K.; Stranks, S. D.; Wang, J. T.-W.; Wojciechowski, K.; Zhang, W. Anomalous Hysteresis in Perovskite Solar Cells. *J. Phys. Chem. Lett.* **2014**, *5*, 1511–1515.
- (17) Tress, W.; Marinova, N.; Moehl, T.; Zakeeruddin, S. M.; Nazeeruddin, M. K.; Grätzel, M. Understanding the Rate-Dependent J-V Hysteresis, Slow Time Component, and Aging in $\text{CH}_3\text{NH}_3\text{PbI}_3$ Perovskite Solar Cells: the Role of a Compensated Electric Field. *Energy Environ. Sci.* **2015**, *8*, 995–1004.
- (18) Bryant, D.; Wheeler, S.; O'Regan, B. C.; Watson, T.; Barnes, P. R. F.; Worsley, D.; Durrant, J. Observable Hysteresis at Low Temperature in Hysteresis Free Organic Inorganic Lead Halide Perovskite Solar Cells. *J. Phys. Chem. Lett.* **2015**, *6*, 3190–3194.
- (19) Heo, J. H.; You, M. S.; Chang, M. H.; Yin, W.; Ahn, T. K.; Lee, S.-J.; Sung, S.-J.; Kim, D. H.; Im, S. H. Hysteresis-Less Mesoscopic $\text{CH}_3\text{NH}_3\text{PbI}_3$ Perovskite Hybrid Solar Cells by Introduction of Li-treated TiO_2 Electrode. *Nano Energy* **2015**, *15*, 530–539.
- (20) Xu, J.; Buin, A.; Ip, A. H.; Li, W.; Voznyy, O.; Comin, R.; Yuan, M.; Jeon, S.; Ning, Z.;

- McDowell, J. J. et al. Perovskite-Fullerene Hybrid Materials Suppress Hysteresis in Planar Diodes. *Nat. Commun.* **2015**, *6*, 7081.
- (21) Li, C.; Tscheuschner, S.; Paulus, F.; Hopkinson, P. E.; Kießling, J.; Köhler, A.; Vaynzof, Y.; Huettnner, S. Iodine Migration and its Effect on Hysteresis in Perovskite Solar Cells. *Adv. Mater.* **2016**, *28*, 2446–2454.
- (22) Xiao, Z.; Yuan, Y.; Shao, Y.; Wang, Q.; Dong, Q.; Bi, C.; Sharma, P.; Gruverman, A.; Huang, J. Giant Switchable Photovoltaic Effect in Organometal Trihalide Perovskite Devices. *Nat. Mater.* **2014**, *14*, 193–198.
- (23) Egger, D. A.; Rappe, A. M.; Kronik, L. Hybrid Organic-Inorganic Perovskites on the Move. *Acc. Chem. Res.* **2016**, *49*, 573–581.
- (24) Yuan, Y.; Huang, J. Ion Migration in Organometal Trihalide Perovskite and Its Impact on Photovoltaic Efficiency and Stability. *Acc. Chem. Res.* **2016**, *49*, 286–293.
- (25) Kutes, Y.; Ye, L.; Zhou, Y.; Pang, S.; Huey, B. D.; Padture, N. P. Direct Observation of Ferroelectric Domains in Solution-Processed CH₃NH₃PbI₃ Perovskite Thin Films. *J. Phys. Chem. Lett.* **2014**, *5*, 3335–3339.
- (26) Fan, Z.; Xiao, J.; Sun, K.; Chen, L.; Hu, Y.; Ouyang, J.; Ong, K. P.; Zeng, K.; Wang, J. Ferroelectricity of CH₃NH₃PbI₃ Perovskite. *J. Phys. Chem. Lett.* **2015**, *6*, 1155–1161.
- (27) Filippetti, A.; Delugas, P.; Saba, M. I.; Mattoni, A. Entropy-Suppressed Ferroelectricity in Hybrid Lead-Iodide Perovskites. *J. Phys. Chem. Lett.* **2015**, *6*, 4909–4915.
- (28) Chen, T.; Foley, B. J.; Ipek, B.; Tyagi, M.; Copley, J. R. D.; Brown, C. M.; Choi, J. J.; Lee, S.-H. Rotational Dynamics of Organic Cations in the CH₃NH₃PbI₃ Perovskite. *Phys. Chem. Chem. Phys.* **2015**, *17*, 31278–31286.
- (29) Mattoni, A.; Filippetti, A.; Saba, M. I.; Delugas, P. Methylammonium Rotational

- Dynamics in Lead Halide Perovskite by Classical Molecular Dynamics: The Role of Temperature. *J. Phys. Chem. C* **2015**, *119*, 17421–17428.
- (30) Frost, J. M.; Walsh, A. What Is Moving in Hybrid Halide Perovskite Solar Cells? *Acc. Chem. Res.* **2016**, *49*, 528–535.
- (31) Yuan, Y.; Chae, J.; Shao, Y.; Wang, Q.; Xiao, Z.; Centrone, A.; Huang, J. Photovoltaic Switching Mechanism in Lateral Structure Hybrid Perovskite Solar Cells. *Adv. Energy Mater.* **2015**, *5*, 1–7.
- (32) Baumann, A.; V  th, S.; Rieder, P.; Heiber, M. C.; Tvingstedt, K.; Dyakonov, V. Identification of Trap States in Perovskite Solar Cells. *J. Phys. Chem. Lett.* **2015**, *6*, 2350–2354.
- (33) Eames, C.; Frost, J. M.; Barnes, P. R. F.; O'Regan, B. C.; Walsh, A.; Islam, M. S. Ionic Transport in Hybrid Lead Iodide Perovskite Solar Cells. *Nat. Commun.* **2015**, *6*, 7497.
- (34) Haruyama, J.; Sodeyama, K.; Han, L.; Tateyama, Y. First-Principles Study of Ion Diffusion in Perovskite Solar Cell Sensitizers. *J. Am. Chem. Soc.* **2015**, *137*, 10048–10051.
- (35) Du, M. H. Efficient Carrier Transport in Halide Perovskites: Theoretical Perspectives. *J. Mater. Chem. A* **2014**, *2*, 9091.
- (36) Duan, H.-S.; Zhou, H.; Chen, Q.; Sun, P.; Luo, S.; Song, T.-B.; Bob, B.; Yang, Y. The Identification and Characterization of Defect States in Hybrid Organic-Inorganic Perovskite Photovoltaics. *Phys. Chem. Chem. Phys.* **2014**, *17*, 112–116.
- (37) Buin, A.; Pietsch, P.; Xu, J.; Voznyy, O.; Ip, A. H.; Comin, R.; Sargent, E. H. Materials Processing Routes to Trap-Free Halide Perovskites. *Nano Lett.* **2014**,

- (38) Yin, W.-J.; Yang, J.-H.; Kang, J.; Yan, Y.; Wei, S.-H. Halide Perovskite Materials for Solar Cells: A Theoretical Review. *J. Mater. Chem. A* **2014**,
- (39) Egger, D. A.; Kronik, L.; Rappe, A. M. Theory of Hydrogen Migration in Organic Inorganic Halide Perovskites. *Angew. Chem. Int. Ed.* **2015**, *54*, 12437–12441.
- (40) Mattoni, A.; Filippetti, A.; Saba, M.; Caddeo, C.; Delugas, P. Temperature Evolution of Methylammonium Trihalide Vibrations at the Atomic Scale. *J. Phys. Chem. Lett.* **2016**, *7*, 529–535.
- (41) Vineyard, G. H. Frequency Factors and Isotope Effects in Solid State Rate Processes. *J. Phys. Chem. Solids* **1957**, *3*, 121–127.
- (42) Allen, M. P.; Tildesley, D. J. *Computer Simulation of Liquids*; Clarendon Press, Oxford, 1989.
- (43) Dualeh, A.; Gao, P.; Seok, S. I.; Nazeeruddin, M. K.; Grätzel, M. Thermal Behavior of Methylammonium Lead-Trihalide Perovskite Photovoltaic Light Harvesters. *Chem. Mater.* **2014**, *26*, 6160–6164.
- (44) Conings, B.; Drijkoningen, J.; Gauquelin, N.; Babayigit, A.; D’Haen, J.; D’Olieslaeger, L.; Ethirajan, A.; Verbeeck, J.; Manca, J.; Mosconi, E. et al. Intrinsic Thermal Instability of Methylammonium Lead Trihalide Perovskite. *Adv. Energy Mater.* **2015**, *5*.
- (45) Tang, M.; Colombo, L.; Zhu, J.; Diaz de la Rubia, T. Intrinsic Point Defects in Crystalline Silicon: Tight-binding Molecular Dynamics Studies of Self-diffusion, Interstitial-Vacancy Recombination, and Formation Volumes. *Phys. Rev. B* **1997**, *55*, 14279–14289.
- (46) Posselt, M.; Gao, F.; Bracht, H. Correlation between Self-Diffusion in Si and the Migration Mechanisms of Vacancies and Self-Interstitials: An Atomistic Study. *Phys. Rev. B* **2008**, *78*, 035208.

- (47) Schie, M.; Marchewka, A.; Müller, T.; De Souza, R. a.; Waser, R. Molecular Dynamics Simulations of Oxygen Vacancy Diffusion in SrTiO₃. *J. Phys. Condens. Matter* **2012**, *24*, 485002.
- (48) Chroneos, A.; Parfitt, D.; Kilner, J. A.; Grimes, R. W. Anisotropic Oxygen Diffusion in Tetragonal La₂NiO_{4+δ}: molecular dynamics calculations. *J. Mater. Chem.* **2010**, *20*, 266–270.
- (49) Islam, M.; Cherry, M.; Catlow, C. Oxygen Diffusion in LaMnO₃ and LaCoO₃ Perovskite-Type Oxides: A Molecular Dynamics Study. *J. Solid State Chem.* **1996**, *124*, 230–237.
- (50) Vaari, J. Molecular Dynamics Simulations of Vacancy Diffusion in Chromium(III) Oxide, Hematite, Magnetite and Chromite. *Solid State Ionics* **2015**, *270*, 10–17.
- (51) Orlandini, S.; Meloni, S.; Ippolito, M.; Colombo, L. Mechanisms of Self-diffusion in Stoichiometric and Substoichiometric Amorphous Silicon Dioxide. *Phys. Rev. B* **2010**, *81*, 014203.